

# Single-dopant band bending fluctuations in MoSe<sub>2</sub> measured with electrostatic force microscopy

Megan Cowie,<sup>1</sup> Rikke Plougmann,<sup>2</sup> Zeno Schumacher,<sup>3</sup> and Peter Grütter<sup>1</sup>

<sup>1</sup>*Department of Physics, McGill University, Montréal, Québec, Canada*

<sup>2</sup>*Department of Physics, Technical University of Denmark, Lyngby, Denmark*

<sup>3</sup>*Department of Physics, Institute of Quantum Electronics, ETH Zurich, 8093 Zürich, Switzerland*

(Dated: October 1, 2021)

In this work, we experimentally demonstrate two-state fluctuations in a metal-insulator-semiconductor (MIS) device formed out of a metallic atomic force microscopy tip, vacuum gap, and multilayer MoSe<sub>2</sub> sample. We show that noise in this device is intrinsically bias-dependent due to the bias-dependent surface potential, and does not require that the frequency or magnitude of individual dopant fluctuations are themselves bias-dependent. Finally, we measure spatial nonhomogeneities in band bending (charge reorganization) timescales.

Individual charge state fluctuations have been observed in a variety of electrically isolated systems such as adatoms[1], quantum dots[2, 3], and molecules[4] on insulators. Understanding these systems is critical for the study of single-electron physics, and two-state systems are of particular relevance for emerging quantum information technology. In semiconducting devices such as photovoltaics, transistors, and diodes, individual charge states such as dangling bonds[5], individual dopants[6], and defects[7] are not electrically isolated from their environment, and it is critical to understand their effects on the global electronic structure, in particular device efficiency and noise. In this work, we measure single dopant fluctuations which give rise to variations in the surface potential of a mesoscopic metal-insulator-semiconductor (MIS) capacitor device. The MIS device is composed of a metallic frequency-modulated atomic force microscopy (fm-AFM) tip, a vacuum gap, and a multilayer MoSe<sub>2</sub> semiconducting sample. The fluctuating two-state effect is demonstrated here for the well-characterized two-dimensional MoSe<sub>2</sub> system, but it has also been observed in pentacene (publication in preparation). This indicates that this is not a sample-specific phenomenon.

The energy of a classical capacitor is found by summing the energies of the charge distributions of each capacitor plate:

$$U_{ts} = \frac{1}{2} \left( \int_t \rho_t(z) V_t(z) dz + \int_s \rho_s(z) V_s(z) dz \right) \quad (1)$$

where the first term is the energy of the top electrode (in this case, the fm-AFM tip) and the second term is the energy of the bottom electrode (MoSe<sub>2</sub> sample). For a metal-insulator-metal capacitor,  $\rho$  and  $V$  are independent of  $z$ , and the expression simplifies to  $U_{ts} = \frac{1}{2} Q_{ts} V_{ts} = \frac{1}{2} C_{ts} V_{ts}^2$ .  $Q_{ts}$  and  $V_{ts}$  are linear with applied bias and  $C_{ts}$  is solely geometric. Deviations from a purely metallic system, such as upon introduction of static charges[8], sample or tip polarizability[9, 10], and surface/interface dipoles[11, 12] can cause  $\rho$  and  $V$  to

vary spatially and have a non-linear bias dependence. This is the case for semiconducting samples, where the surface potential  $V_S$  that is established by the charge  $Q_S$  inside a semiconductor is bias-dependent and spatially non-uniform (thus the potential that arises due to band bending.) In this work,  $V_S$  has been calculated by numerically solving the following equation[13]:

$$V_S = V_{bias} + V_{CPD} - \frac{Q_S}{C_I} \quad (2)$$

where  $Q_S = Q_S(V_S)$  and  $C_I$  is the (geometric) capacitance per unit area, found by solving the Poisson Equation (see Supplemental Material at [] for this derivation). The total charge density is composed of thermal carriers, ionized dopants, and “effective dopants”, which are generically any ionizable states such as surface states, interface traps[14], point vacancies[15], contaminants, adatoms, interstitial atoms[16], etc. This incorporation of ionized “effective dopant” states into the total charge density means that even an undoped sample can behave as though it were doped if other contributing effective dopant densities are appreciable. The occupation of dopant (or effective dopant) states can vary due to charge transfer from other sample locations, such as the substrate or interstitial contamination layers[17]. The MIS force per unit area  $a_{tip}$  (derived in Hudlet *et al* 1995[13]) is:

$$\frac{F_{ts}}{a_{tip}} = \frac{Q_S^2}{2\epsilon} \quad (3)$$

Figures 1a,b show the bias dependence of  $V_S$  and  $F_{ts}$ , where each point is a numerical solution to Equations 2 and 3. The non-linear surface potential  $V_S$  leads to a nonparabolicity in the force  $F_{ts}$ .

In fm-AFM, a tip mounted on a cantilever (spring constant  $k$ , Q-factor  $Q$ ) oscillates sinusoidally above a sample surface ( $z = A \sin(\omega t)$ ). Tip-sample force ( $F_{ts}$ ) contributions which are in-phase with the cantilever motion

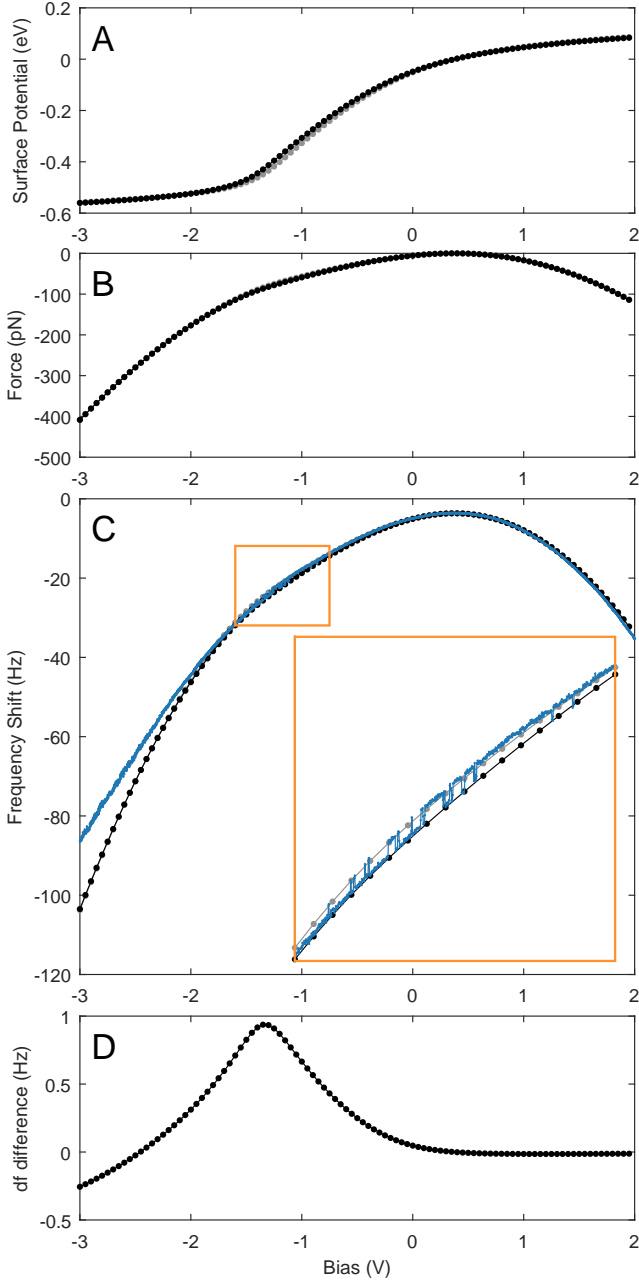


FIG. 1. a) Modelled bias dependence of the MIS surface potential (Equation 2) and b) force (Equation 3). c) Modelled frequency shift (black, Equation 4a) and fm-AFM frequency shift data (blue) on multilayer MoSe<sub>2</sub>. Inset: A zoom-in of the frequency shift (yellow rectangle) for which fluctuations in the data (blue) were observed. These fluctuations were modeled as the system fluctuating between two ionized acceptor concentrations:  $6.3 \times 10^{17}/\text{cm}^3$  (black) and  $7.1 \times 10^{17}/\text{cm}^3$  (grey). d) The difference between the two models (grey and black) shown in c, inset as a function of bias. (This is effectively a “noise sensitivity function”.) The experimental and model parameters for (a-d) are given in the main text. The sweep was acquired over approximately 10 seconds, and the bandwidth of the phase-locked-loop was 305 Hz.

lead to shifts in the cantilever resonant frequency ( $\Delta\omega$ ) and out-of-phase force contributions lead to variations in the cantilever drive, or excitation, required to maintain constant oscillation amplitude  $A$ :

$$\Delta\omega = \omega - \omega_o = \frac{-\omega_o \omega_o}{2kA} \frac{1}{\pi} \int_0^{2\pi/\omega} F_{ts}(t) \sin(\omega t) dt \quad (4a)$$

$$F_d = \frac{kA}{Q} - \frac{\omega_o}{\pi} \int_0^{2\pi/\omega} F_{ts}(t) \cos(\omega t) dt \quad (4b)$$

(see Supplemental Material at [] for a derivation of Equation 4.) The nonparabolicity in the force  $F_{ts}$  which arises due to the nonlinearity in surface potential  $V_S$  leads to a nonparabolic fm-AFM frequency shift above MoSe<sub>2</sub> (Figure 1c). Recently, similar nonparabolicities have been reported in other systems measured with fm-AFM, including dangling bonds on Si(111)[5] and pentacene on KBr[18]. Reference measurements on SiO<sub>2</sub>, in contrast, show a parabolic frequency shift as a function of bias. (See Supplemental Material at [] for these measurements.)

The inset of Figure 1c shows a zoom-in of the kink in the frequency shift parabola. At these biases, the measured frequency shift (blue) fluctuates between two states. This is due to individual dopant fluctuations which cause variations in  $Q_S$ . The two model fits shown differ only in their acceptor concentration, which are  $6.3 \times 10^{17}/\text{cm}^3$  (black) and  $7.1 \times 10^{17}/\text{cm}^3$  (grey). This is a dopant concentration difference of  $0.8 \times 10^{17}/\text{cm}^3$ , which corresponds to approximately one charge within the estimated  $2.8 \times 10^{-18} \text{ cm}^3$  tip probing volume, assuming a probe volume equal to the effective tip area ( $\pi \times 10^2 \text{ nm}^2$ ) times the sample thickness (9 nm). This fluctuation effect does not manifest homogeneously over the sample surface: Rather, it is only present at certain locations, and vanishes when the tip is moved slightly (50 nm). The measured frequency shift fluctuation is maximized at biases corresponding to the kink in the surface potential ( $\sim -1.4 \text{ V}$ ). This is demonstrated in Figure 1d, which shows the difference between the two fits in Figure 1c. Figure 1d signifies that the bias dependence of the fluctuation amplitude is due to an amplification of the measured fluctuating signal at these biases, and is not due to a bias dependence in the occupation of dopant states. See Supplemental Materials at [] for a further explanation. Note that band bending in thin samples is spatially limited in the  $z$  (perpendicular) direction, but if there is a localized gate (as is the case for fm-AFM), band bending also occurs in the  $x$  and  $y$  directions, meaning that there can still be an appreciable surface potential[6, 18]. This is why previously-reported defects measured with fm-AFM on thin TMDC samples[7] are much larger than a single lattice site.

Figure 2 shows the excitation signal measured simultaneously with the frequency shift data shown in Figure 1c.

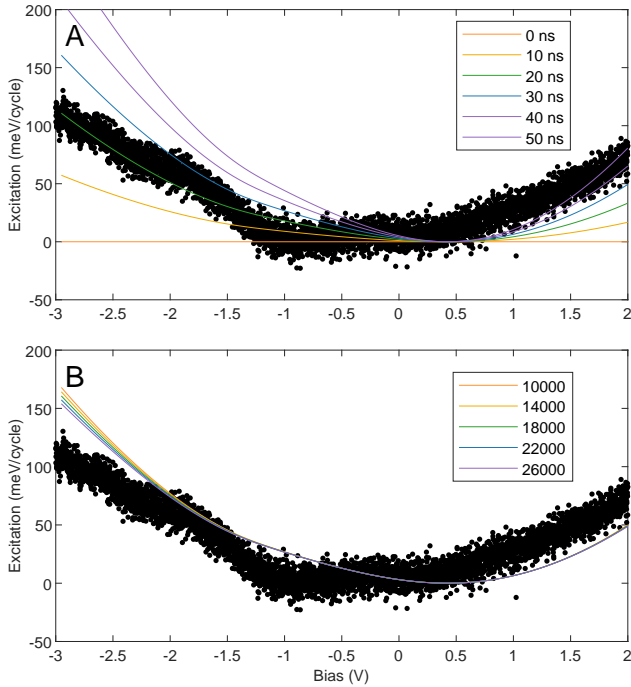


FIG. 2. Modeled excitation signal as a function of bias with a) constant Q-factor (18000); and b) constant lag (30 ns). The other parameters match those defined in the previous section of this work. Experimental results from Figure 1 are shown in black.

The non-constant excitation signifies an out-of-phase tip-sample force  $F_{ts}$ , according to Equation 4b. Supplemental Material at [] shows that reference measurements on  $\text{SiO}_2$  show constant excitation as a function of bias.) This out-of-phase component arises from charge reorganization inside the sample, or in other words, it is an equilibration timescale for the surface potential. Modeled lag times ranging from 0 to 50 ns are shown in Figure 2a. The best estimate of this band bending timescale is 30 ns. This timescale is effectively an RC time constant for the tip-vacuum-sample MIS system. An order-of-magnitude estimate of the time constant  $\tau = RC$ , assuming a simple parallel-plate capacitor  $C = \frac{\epsilon\epsilon_0 A}{d}$  and resistivity  $\rho = \frac{RA}{d}$ , agrees with this model: Using the best-fit relative permittivity from this work ( $\epsilon = 5.9$ ) and a resistivity of 500  $\Omega m$  (which is within the wide reported resistivity range of 0.1 – 1000  $\Omega m$  for  $\text{MoSe}_2$ [19]), gives  $\tau = 26$  ns, which is consistent with the best estimate value shown in Figure 2a. The model appears to be simplistic as the fit misses many details of the data; this could be due to a bias-dependent lag time, which has not been accounted for here. Nonetheless this explanation can be useful for an order-of-magnitude estimate of the band-bending timescale. Note that when the lag is zero, the excitation signal is flat, and this is independent of Q. Furthermore, Figure 2b demonstrates that this excitation signal does not arise from variations in Q as a func-

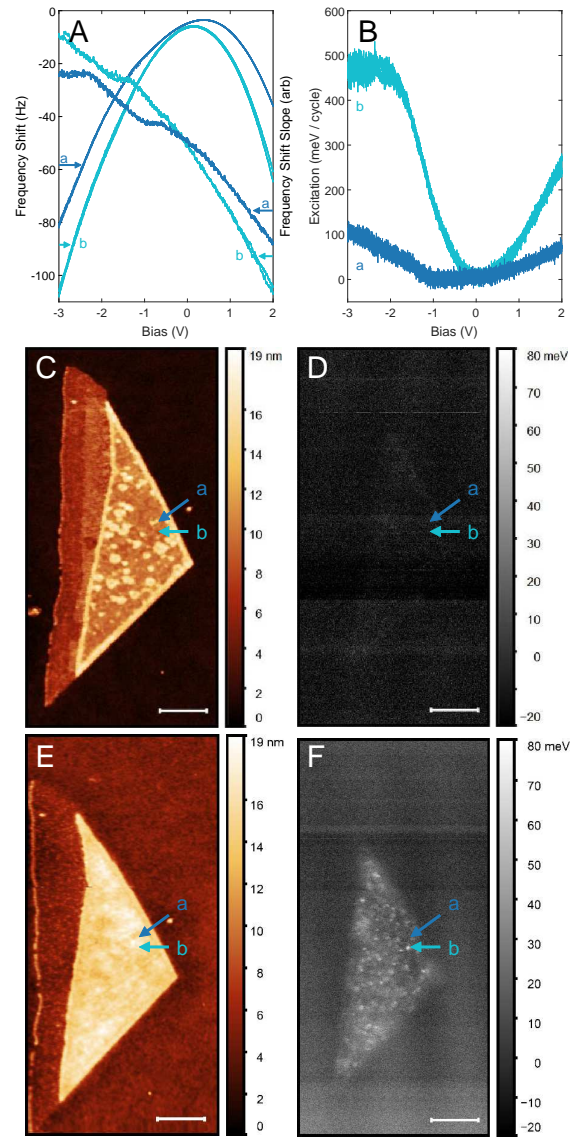


FIG. 3. a,b) Frequency shift and excitation bias spectra taken at two locations labeled ‘a’ and ‘b’, separated by 50 nm. c,d) Frequency shift and excitation fm-AFM images at 0V and e,f) -1.5V. Note that there is no correlation between the excitation spots and PMMA residues (bright spots in the 0V z channel image). The horizontal scale bar corresponds to 500 nm.

tion of bias, since large variations in Q at a constant lag time (30 ns) do not reproduce the measured phenomenon. This confirms that the measured excitation signal is not due to ‘dissipation’ (i.e. a non-conservative force, which would change Q), but rather a time-delayed conservative force.

The excitation channel can be measured spatially to map variations in band bending timescales over a sample surface. This is demonstrated in Figure 3, which shows frequency shift and excitation bias spectra (a-b) at two locations, as well as frequency shift and excitation images measured at 0 V (c-d) and -1.5 V (e-f). The two

positions are separated by approximately  $50\text{ nm}$ . The highest layer of the island, susceptible geometrically to the largest surface potential since it is not so spatially limited in the  $z$  direction, exhibits the most appreciable bias dependence. Bright spots become visible in the excitation channel, indicating a spatial nonhomogeneity in the charge equilibration time. We note that Figures 3a and b confirm that this observation of bias-dependent excitation is not a piezoacoustic excitation system transfer function artefact such as described in Labuda *et al* (2011)[20], since by changing the position slightly on the sample, the frequency shift and excitation vary independently. This excitation signal is also not due to tunneling charge transfer between the sample and tip, since the effect was observed at tip-sample separations  $> 5\text{ nm}$  larger than that shown in Figure 2.

## METHODS

*Experimental Parameters* – The sample of  $\text{MoSe}_2$  on  $\text{SiO}_2$  measured in this work was prepared by all-dry viscoelastic stamping[21]. The top layer of a micron-scale multilayer island of  $\text{MoSe}_2$ , shown imaged with Kelvin probe force microscopy (KPFM) in Figure 4, is  $9.0 \pm 0.4\text{ nm}$  above the silicon substrate. (This was measured by applying Gaussian fits to histograms of the total substrate and top layer areas and subtracting their means, see [22] for more details.) The spots that are visible on the island KPFM image (Figure 4b) are likely PMMA stamping/transfer residues[22]. These residues do not appear to significantly modify the underlying  $\text{MoSe}_2$  electronic structure (see Figure 3d,f) but

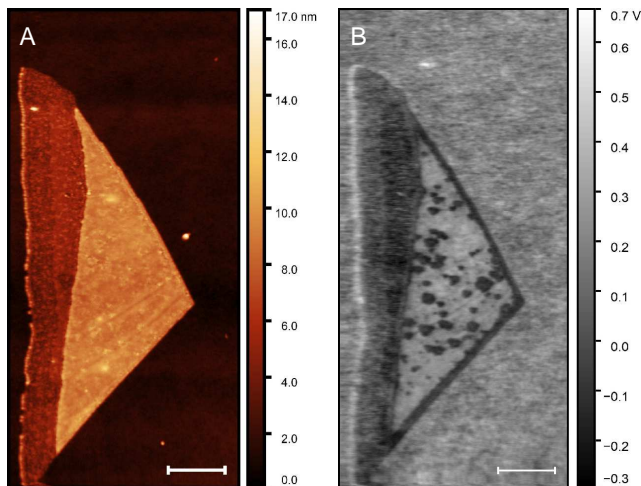


FIG. 4. Single-pass fm-KPFM image of a micron-scale stepped island of  $\text{MoSe}_2$ . a) The ‘height’ channel ( $z$ -piezo extension to maintain constant cantilever frequency). b) The simultaneous KPFM DC bias compensation. The horizontal scale bar corresponds to  $500\text{ nm}$ .

rather in effect provide an extra insulating layer in the tip-sample junction. All fm-AFM measurements were taken using Nanosensors platinum-iridium coated silicon tips (PPP-NCHPt) with  $330\text{ kHz}$  resonant frequency, spring constant  $42\text{ N/m}$ , and  $Q$  factors approximately 18000 in a JEOL JSPM-4500A UHV AFM with a Nanonis control system. All measurements were performed in ultra-high vacuum (base pressure  $< 3 \times 10^{-10}\text{ mbar}$ ) at room temperature. Samples were annealed at  $120^\circ\text{C}$  for eight hours after being introduced into vacuum.

*Model Description* – Figure 5 illustrates how the tip-sample force, and therefore the frequency shift and dissipation, depend on the surface potential (band bending). Over every oscillation cycle, the tip-sample separation changes, the potential drop across the vacuum gap changes, and the potential drop inside the semiconductor changes, resulting in an oscillating surface potential and force. A non-zero band bending timescale means that there is a phase offset between the closest tip-sample position and the maximum tip-sample force, and therefore (Equation 4b) there is a non-zero excitation signal. See Supplemental Material at [] for a video depiction of Figure 5 demonstrating how the band diagram changes over every oscillation cycle. The frequency shift and excitation curves modeled in Figures 1c and 2 are calculated by integrating the force vs. time curve  $F_{ts}(t)$  (Figure 5f) according to Equation 4. Each model point shown in Figures 1a-c and 2 is a solution to Equations 2, 3, and 4 at a different bias.

*Model Parameters* – Equations 2, 3, and 4 involve 14 experimental parameters, but the impact each has on the overall parabola shape is distinct. The band gap and acceptor concentration have the largest impact for introducing nonparabolicity, and the permittivity and temperature are not as sensitive parameters, yet play similar roles. The tip work function and sample electron affinity simply introduce lateral shifts in the force curve, and leave the shape unchanged. The tip-sample separation, tip radius, oscillation amplitude and frequency, spring constant, and  $Q$ -factor are all fm-AFM scaling factors that are multiplicative prefactors which are required to convert between force and frequency shift, but which do not change the overall shape. See Supplemental Material at [] for a further explanation of the sensitivity of each of these parameters and their impact on the shape. Optimal fit values were found by exploring a large parameter space ( $> 120,000$  curves) and finding the fit that minimizes residuals. The few-layer  $\text{MoSe}_2$  band gap is  $1.55\text{ eV}$ [20, 23] (best fit  $1.5\text{ eV}$ ), electron affinity  $3.5\text{ eV}$ [24] (no fit against this parameter), and relative (dielectric) permittivity  $5.7$ [25] (best fit  $5.9$ ). A rigorous interpretation of permittivity is challenging because there is likely water in between the thin flaked  $\text{MoSe}_2$  sample and the  $\text{SiO}_2$  substrate. However, the permittivity is a relatively less sensitive parameter, so taking this fitted permittivity as an “effective permittivity” of the net sys-

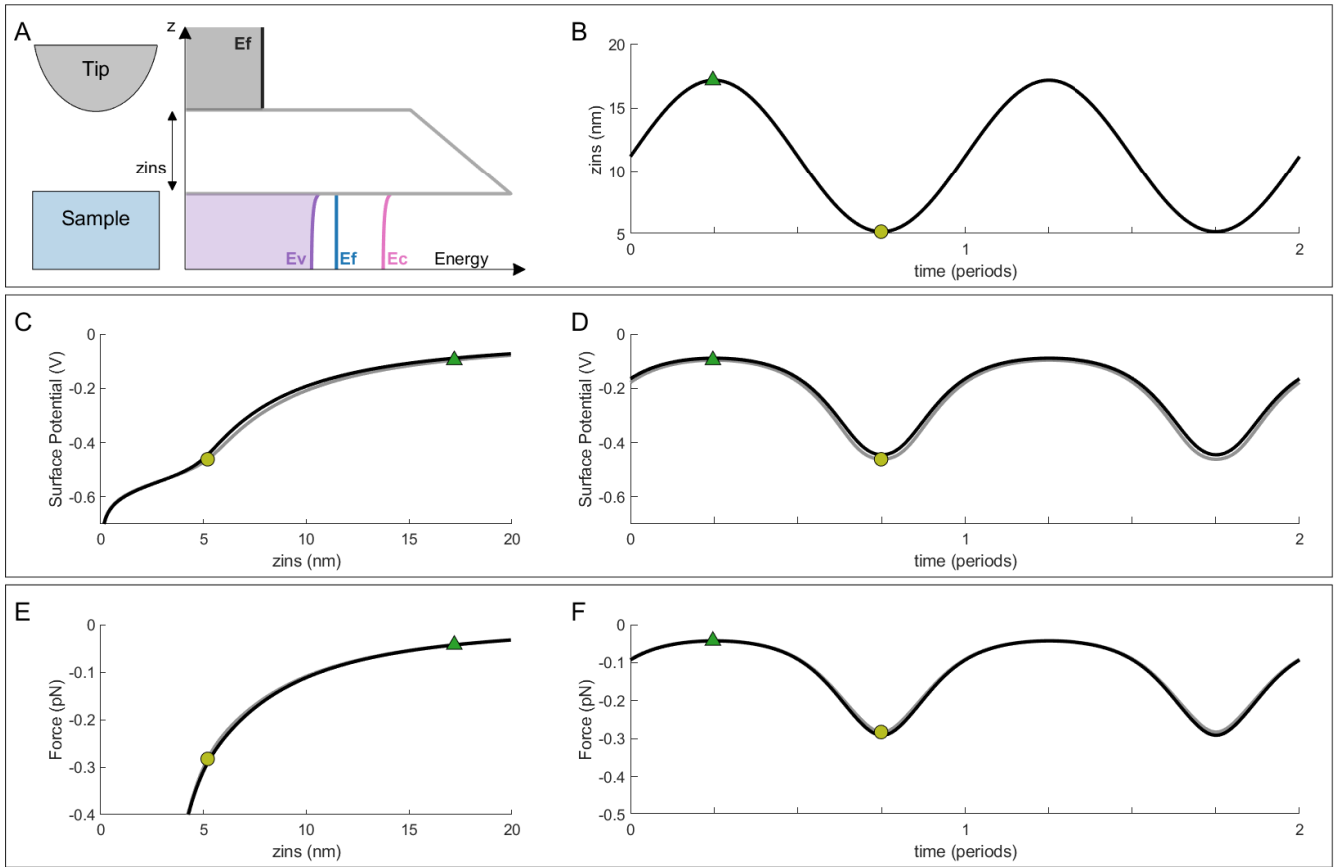


FIG. 5. Simulation of the origin of a fm-AFM force measured over a semiconducting sample at a bias of  $-1.5$  V for two acceptor concentrations:  $6.3e17/cm^3$  (black) and  $7.1e17/cm^3$  (grey). (The remaining parameters values are the best fit values defined in the text.) a) Schematic of the fm-AFM setup corresponding to a band diagram of a MIS capacitor oriented along the  $z$ -axis. Pink ( $E_c$ ) and purple ( $E_v$ ) are the sample conduction and valence bands, blue ( $E_f$ ) shows the sample Fermi level, dark grey ( $E_f$ ) shows metallic tip (gate) Fermi level, and light grey demonstrates the potential drop across the insulator (vacuum). b) Time trace showing that the thickness of the insulator  $z_{ins}$  (i.e. tip-sample separation) varies sinusoidally over every oscillation cycle. c,d) The surface potential as a function of  $z_{ins}$  and time. e,f) The tip-sample force as a function of  $z_{ins}$  and time. Two points, a light green circle and a dark green triangle, are shown for b-f to clarify the relationship between each subfigure. See Supplemental Material at [] for an animated version of this figure.

tem does not affect the overall interpretation. The effective electron and hole masses were assumed to be 1.0, and the temperature 300 K. The spring constant of 42 N/m was estimated by the tip manufacturer, and the best fit was in agreement with 42 N/m. The Q-factor and resonant frequency were measured experimentally by performing a frequency sweep; they are 18000 and 330 kHz, respectively. The oscillation amplitude setpoint, maintained with a phase-locked loop and a feedback circuit, was 6 nm. See the Supplemental Material at [] for the reference measurement on SiO<sub>2</sub> that was used to estimate the tip work function: The work function of the Si/SiO<sub>2</sub> is 4.4 eV, and given that the substrate parabola peak (i.e.  $V_{CPD}$ , see Figure 1) is 400 mV, the tip work function ( $V_{CPD} = \Phi_{tip} - \Phi_{sample}$ ) is 4.0 eV (best fit 4.1 eV). The closest tip-sample separation (i.e. the MIS capacitor insulator thickness) and effective tip radius both identi-

cally effect the frequency shift curvature, so for fitting the tip radius was fixed (10 nm) and the optimal  $z_{ins}$  was 5.2 nm. The 10 nm tip radius fit is reasonable, since the tip manufacturers quote an effective radius “better than 25 nm”. The position of the experimental parabola kink at negative biases (highlighted with a yellow rectangle in Figure 1c) indicates that the effective dopants are p-type. The dopant concentration, the final fitting parameter, is optimized at  $6.3e17/cm^3$  (black) and  $7.1e17/cm^3$  (grey). The frequency shift fits shown in Figures 1c-e appear to fit the data well, except for a deviation at large negative biases. This could be due to the emergence of stray capacitances as the applied electric field increases. See Supplemental Material at [] for a demonstration of the sensitivity of this parameter space.

In conclusion, we have experimentally resolved individual dopant fluctuations which influence the global band

bending of a mesoscopic MIS device. The bias dependence of these fluctuations does not depend on the bias dependence of the dopant state occupation, but is rather inherently due to the bias dependence of the surface potential. This bias-dependent fluctuation – and, consequently for small devices, this bias-dependent noise – occurs even for bias-independent thermally ionized states. This has important ramifications for MIS-like device functionality and noise: It indicates that even in the absence of bias-dependent dopant or defect states, device noise is bias dependent. There is a timescale required for the surface potential to reach equilibrium, which can be measured using the excitation channel in fm-AFM. This may be used to explore band bending timescales of different types of defects, as well as the emergence of  $1/f$  noise in mesoscopic systems.

We thank NSERC, FRQ-NT and CFI for funding, Alexander Schluger, Kirk Bevan, and Hong Guo for stimulating discussions, and Philipp Nagler for the preparation of the MoSe<sub>2</sub> sample.

- 
- [1] L. Gross, F. Mohn, P. Liljeroth, J. Repp, F. Giessibl, and G. Meyer, Measuring the charge state of an adatom with noncontact atomic force microscopy, *Science* **324**, 1428 (2009).
- [2] S. Bennett, L. Cockins, Y. Miyahara, P. Grütter, and A. Clerk, Strong electromechanical coupling of an atomic force microscope cantilever to a quantum dot, *Physical Review Letters* **104**, 017203 (2010).
- [3] A. Roy-Gobeil, Y. Miyahara, and P. Grütter, Revealing energy level structure of individual quantum dots by tunneling rate measured by single-electron sensitive electrostatic force spectroscopy, *Nano Letters* **15**, 2324–2328 (2015).
- [4] A. Roy-Gobeil, Y. Miyahara, K. Bevan, and P. Grütter, Fully quantized electron transfer observed in a single redox molecule at a metal surface, *Nano Letters* **19**, 6104–6108 (2019).
- [5] N. Turek, S. Godey, D. Deresmes, and T. Mélin, Ring charging of a single silicon dangling bond imaged by noncontact atomic force microscopy, *Physical Review B* **102**, 235433 (2020).
- [6] K. Teichmann, M. Wenderoth, S. Loth, R. G. Ulbrich, J. K. Garleff, A. P. Wijnheijmer, and P. M. Koenraad, Controlled charge switching on a single donor with a scanning tunneling microscope, *Physical Review Letters* **101**, 076103 (2008).
- [7] R. Plumadore, M. Baskurt, J. Boddison-Chouinard, G. Lopinski, M.n Modarresi, P. Potasz, P. Hawrylak, H. Sahin, F. M. Peeters, and A. Luican-Mayer, Prevalence of oxygen defects in an in-plane anisotropic transition metal dichalcogenide, *Physical Review B* **102**, 205408 (2020).
- [8] L. N. Kantorovich, A. I. Livshits, and M. Stoneham, Electrostatic energy calculation for the interpretation of scanning probe microscopy experiments, *Journal of Physics: Condensed Matter* **12**, 795 (2000).
- [9] S. A. Burke, J. M. LeDue, Y. Miyahara, J. M. Topple, S. Fostner, and P. Grütter, Determination of the local contact potential difference of PTCDA on NaCl: a comparison of techniques, *Nanotechnology* **20**, 264012 (2009).
- [10] J. Zhang, W. Lu, Y. S. Li, J. Cai, and L. Chen, Dielectric force microscopy: Imaging charge carriers in nanomaterials without electrical contacts, *Accounts of Chemical Research* **48**, 1788 (2015).
- [11] M. Schmeits, Electrical conduction in semiconductor junctions with interface dipole layers, *Journal of Applied Physics* **80**, 941 (1996).
- [12] C. León, H. Drees, S. M. Wippermann, M. Marz, and R. Hoffmann-Vogel, Atomic-scale imaging of the surface dipole distribution of stepped surfaces, *Physical Chemistry Letters* **7**, 426–430 (2016).
- [13] S. Hudlet, M. Saint Jean, B. Roulet, J. Berger, and C. Guthmann, Electrostatic forces between metallic tip and semiconductor surfaces, *Journal of Applied Physics* **77**, 3308 (1995).
- [14] M.J. Kirton and M.J. Uren, Noise in solid-state microstructures: A new perspective on individual defects, interface states, and low-frequency ( $1/f$ ) noise, *Advances in Physics* **38**, 367 (1989).
- [15] H-P. Komsa, J. Kotakoski, S. Kurasch, O. Lehtinen, U. Kaiser, and A. V. Krasheninnikov, Two-dimensional transition metal dichalcogenides under electron irradiation: defect production and doping, *Physical Review Letters* **109**, 035503 (2012).
- [16] S-Y. Seo, D-H. Yang, G. Moon, O. F. N. Okello, M. Yeong Park, S-H. Lee, S-Y. Choi, and M-H. Jo, Identification of point defects in atomically thin transition-metal dichalcogenide semiconductors as active dopants, *Nano Letters* **21**, 3341 (2021).
- [17] E. Pollmann, L. Madau, S. Schumacher, U. Kumar, F. Heuvel, C. vom Ende, S. Yilmaz, S. Güngörmüş, and M. Schleberger, Apparent differences between single layer molybdenum disulphide fabricated via chemical vapour deposition and exfoliation, *Nanotechnology* **31**, 505604 (2020).
- [18] Z. Schumacher, R. Rejali, M. Cowie, A. Spielhofer, Y. Miyahara, and P. Grütter, Charge carrier inversion in a doped thin film organic semiconductor island, *ACS Nano* **15**, 10377–10383 (2021).
- [19] X. Zhu, Z. Zhou, Y. Wang, L. Zhang, A. Li, F. Huang, Determining factor of MoSe<sub>2</sub> formation in Cu(In,Ga) Se<sub>2</sub> solar cells, *Solar Energy Materials & Solar Cells* **101**, 57 (2012).
- [20] A. Labuda, Y. Miyahara, L. Cockins, and P. Grütter, Decoupling conservative and dissipative forces in frequency modulation atomic force microscopy, *Physical Review B* **84**, 125433 (2011).
- [21] A. Castellanos-Gomez, M. Buscema, R. Molenaar, V. Singh, L. Janssen, H. S. J. van der Zant, and G. A. Steele, Deterministic transfer of two-dimensional materials by all-dry viscoelastic stamping, *2D Materials* **1**, 01102 (2014).
- [22] R. Plougmann, M. Cowie, Y. Benkirane, L. Schuè, Z. Schumacher, and P. Grütter, How high is a MoSe<sub>2</sub> monolayer?, Manuscript under review <https://arxiv.org/abs/2109.05354> (2021).
- [23] Y. Miyahara, J. Topple, Z. Schumacher, and P. Grütter, Kelvin probe force microscopy by dissipative electrostatic force modulation, *Physical Review Applied* **4**, 054011 (2015).
- [24] L.N. Kantorovich and T. Trevethan, General theory of microscopic dynamical response in surface

- probe microscopy: From imaging to dissipation, *Physical Review Letters* **93**, 236102 (2004).
- [25] H. Hölscher, B. Gotsmann, W. Allers, U. D. Schwarz, H. Fuchs, and R. Wiesendanger, Measurement of conservative and dissipative tip-sample interaction forces with a dynamic force microscope using the frequency modulation technique, *Physical Review B* **64**, 075402 (2001).
- [26] J. E. Sader, T. Uchihashi, M. J. Higgins, A. Farrell, Y. Nakayama, and S. P. Jarvis, Quantitative force measurements using frequency modulation atomic force microscopy—theoretical foundations, *Nanotechnology* **16**, S94–S101 (2005).
- [27] H. J. Hug and A. Baratof, *Noncontact atomic force microscopy* (Springer International Publishing, 2002) Chap. 20, pp. 395–431.
- [28] J. Lindmayer, Field effect studies of the oxidized silicon surface, *Solid-State Electronics* **9**, 225 (1966).
- [29] S. Sadewasser and T. Glatzel, *Kelvin probe force microscopy: From single charge detection to device characterization* (Springer International Publishing, 2018).
- [30] S. Tongay, J. Zhou, C. Ataca, K. Lo, T. S. Matthews, J. Li, J. C. Grossman, and J. Wu, Thermally driven crossover from indirect toward direct bandgap in 2D semiconductors: MoSe<sub>2</sub> versus MoS<sub>2</sub>, *Nano Letters* **12**, 5576 (2012).
- [31] Choi, B.K. *et al*, Temperature dependence of band gap in MoSe<sub>2</sub> grown by molecular beam epitaxy, *Nanoscale Research Letters* **12**, 492 (2017).
- [32] B. K. Choi, M. Kim, K-H. Jung, J. Kim, K-S. Yu, and Y. J. Chang, Computational search for two-dimensional MX<sub>2</sub> semiconductors with possible high electron mobility at room temperature, *Nanoscale Research Letters* **9**, 716 (2017).
- [33] Q. Zhang, S. Zhang, B. A. Sperling, and N. V. Nguyen, Band offset and electron affinity of monolayer MoSe<sub>2</sub> by internal photoemission, *Journal of Electronic Materials* **48**, 6446–6450 (2019).
- [34] K-K. Kam, *Electrical properties of WSe<sub>2</sub>, WS<sub>2</sub>, MoSe<sub>2</sub>, MoS<sub>2</sub>, and their use as photoanodes in a semiconductor liquid junction solar cell*, Ph.D. thesis, Iowa State University (1982).
- [35] M.K. Agarwal, P.D. Patel, and S.K. Gupta, Effect of doping MoSe<sub>2</sub> single crystals with rhenium, *Journal of Crystal Growth* **129**, 559 (1993).

# Supplementary Materials

## SURFACE POTENTIAL AND FORCE

When a bias is applied to a semiconductor, its finite density of states means that there is a spatially-dependent electric field inside the semiconductor. This causes charge within the semiconductor to re-organize, and creates a spatially dependent potential that decays with distance (band bending). The amount of band bending, that is, the difference between the bulk potentials and the potential at the surface, is the surface potential, and is calculated by solving the Poisson equation:

$$\frac{\partial \vec{E}}{\partial z} = -\nabla^2 V = \frac{\rho}{\epsilon} \quad (5)$$

where the total charge density in the semiconductor  $\rho$  is generally taken to be due to the thermally excited carriers ( $n(z)$ ,  $p(z)$ ) and ionized dopants ( $n_D^+$ ,  $n_A^-$ ):

$$\rho = e (n(z) - p(z) + n_D^+ - n_A^-) \quad (6)$$

Imperfect (real-world) samples with surface or defect states, such as edge states, dangling bond states, etc, can have additional carriers contributed by either filling ( $p_s$ ) or depleting ( $n_s$ ) defect states, just as dopants do. A robust definition of  $\rho$  therefore includes these contributions:

$$\begin{aligned} \rho &= e (n(z) - p(z) + n_D^+ - n_A^- + n_d^+ + n_a^-) \\ &= e (n(z) - p(z) + n_{D,d}^+ - n_{A,a}^-) \end{aligned} \quad (7)$$

such that the Poisson equation is:

$$\frac{\partial \vec{E}}{\partial z} = \frac{e}{\epsilon} (n(z) - p(z) + n_{D,d}^+ - n_{A,a}^-) \quad (8)$$

The charge inside the semiconductor is:

$$Q_s = \text{sgn}(u) \frac{\epsilon \epsilon_o k_B T}{e L_D} \left[ e^u - u - 1 + \frac{n_i^2}{N_A^2} (e^{-u} + u - 1) \right]^{1/2} \quad (9)$$

where  $u = \frac{eV_s}{k_B T}$  and  $L_D = \sqrt{\frac{\epsilon \epsilon_o k_B T}{2 N_A e^2}}$ . The surface potential is found by solving the following continuity equation numerically:

$$0 = V_{bias} + V_{CPD} - V_S - \frac{Q_S \times z_{ins}}{\epsilon_o} \quad (10)$$

where  $V_{CPD} = E_{f,t} - E_{f,s}$  and  $E_{f,t}$  and  $E_{f,s}$  are the tip and sample Fermi levels, respectively. Finally, the net tip-sample force is found algebraically given the  $V_S$  solution:

$$F_{ts} = a_{tip} \times \frac{Q_S^2}{2\epsilon_o} \quad (11)$$

where  $a_{tip} = \pi r_{tip}^2$  is the effective tip area. This derivation is shown in greater detail in Hudlet *et al* (1995)[13]. (Note that the expressions have been modified slightly to account for the fact that this system is p-type, and accounting for the fact that the tip and sample have different Fermi levels.)

## FREQUENCY SHIFT AND DISSIPATION

The following section demonstrates that in an fm-AFM experiment, the frequency shift arises from the in-phase component of the tip-sample force, while variations in excitation arises from the out-of-phase component. (This derivation is also presented elsewhere[23–26], but is shown here for clarity.) In the small amplitude limit, an fm-AFM cantilever behaves like a damped, driven harmonic oscillator with equation of motion:

$$m\ddot{z} + \xi\dot{z} + kz = F_{drive} + F_{ts}(z, t) \quad (12)$$

where  $m$  is the cantilever mass,  $\xi$  is the damping coefficient,  $k$  is the spring constant,  $F_{drive}$  is the driving force, and  $F_{ts}(z, t)$  is the tip-sample interaction force. Rewritten in terms friendlier to an experimentalist, given that the cantilever resonance frequency  $\omega_o = \sqrt{\frac{k}{m}}$  and quality factor  $Q = \frac{m\omega_o}{\xi}$ , we have:

$$k\ddot{z} + \frac{k\omega_o}{Q}\dot{z} + k\omega_o^2 z = \omega_o^2(F_{drive} + F_{ts}(z, t)) \quad (13)$$

We can solve the equation of motion using the ansatz  $z = A \sin(\omega t)$ .  $F_{drive}$ . The drive, which when optimized is 90 degrees out of phase with the position, is  $F_{drive} = F_d \cos(\omega t)$ , such that:

$$F_{ts}(t) = \left[ \frac{kA}{\omega_o^2}(\omega_o^2 - \omega^2) \right] \sin(\omega t) + \left[ \frac{kA}{\omega_o^2} \frac{\omega\omega_o}{Q} - F_d \right] \cos(\omega t) \quad (14)$$

The total force  $F_{ts}$  can be generically expressed as a Fourier series with the orthonormal basis of  $\sin(t)$  and  $\cos(t)$ . Taking only the terms at frequency  $\omega$ , we find that the force can be expressed as:

$$F_{ts}(t) = F_{in} \sin(\omega t) + F_{out} \cos(\omega t) \quad (15)$$

where the amplitudes of the in-phase and out-of-phase force contributions are the Fourier coefficients:

$$F_{in} = \frac{\omega}{\pi} \int_0^{2\pi/\omega} F_{ts}(t) \sin(\omega t) dt \quad (16a)$$

$$F_{out} = \frac{\omega}{\pi} \int_0^{2\pi/\omega} F_{ts}(t) \cos(\omega t) dt \quad (16b)$$

Therefore we can separate Equation 14 into its orthogonal components and rearrange to find the frequency shift ( $\Delta\omega$ ) and drive amplitude ( $F_d$ ) given any generic tip-sample interaction  $F_{ts}$  in the regime where  $\omega \approx \omega_o$ :

$$\Delta\omega = \omega - \omega_o = \frac{-\omega_o}{2kA} \frac{\omega_o}{\pi} \int_0^{2\pi/\omega} F_{ts}(t) \sin(\omega t) dt \quad (17a)$$

$$F_d = \frac{kA}{Q} - \frac{\omega_o}{\pi} \int_0^{2\pi/\omega} F_{ts}(t) \cos(\omega t) dt \quad (17b)$$

Consequently, that component of the tip-sample force that is in phase with the cantilever position shifts the cantilever resonant frequency, and the out-of-phase component of the force contributes to the drive signal. Finally, in the regime where  $\omega \approx \omega_o$  the drive signal may be expressed as an energy loss per cycle as[27]:

$$E_{ts} = E_o \left[ \frac{F_d - F_{do}}{F_d} \right] \quad (18)$$

where  $E_o = \frac{\pi k a^2}{Q}$  is the intrinsic damping loss of a high quality factor oscillator[27] and  $F_{do} = \frac{kA}{Q}$  is the offset in Equation 4b. Experimental drive signals are also converted to units of energy loss per cycle given the above expression, where  $F_d = A_{exc}$  is the measured drive amplitude Volts and  $F_{do} = A_{exco}$  is the drive amplitude in Volts measured in the absence of a tip-sample interaction.

## FITS

Of the total fourteen experimental parameters in this fit, only three material parameters affect the overall shape of the frequency shift. These are the band gap  $E_g$ , acceptor concentration  $N_A$ , and permittivity  $\epsilon$ . The tip work function and sample electron affinity simply provide lateral shifts (Equation 10) in the frequency shift and leave the shape unchanged. There are six fmAFM-specific parameters (tip-sample separation  $z_{ins}$ , tip radius  $r_{tip}$ , oscillation amplitude  $A$ , oscillation frequency  $\omega$ , spring constant  $k$ , and Q-factor  $Q$ ) which all are simply scaling constants (see Equations 11 and 17a). Slight variations around the best fit values for each of these parameters are shown in Figures 6 and 7,

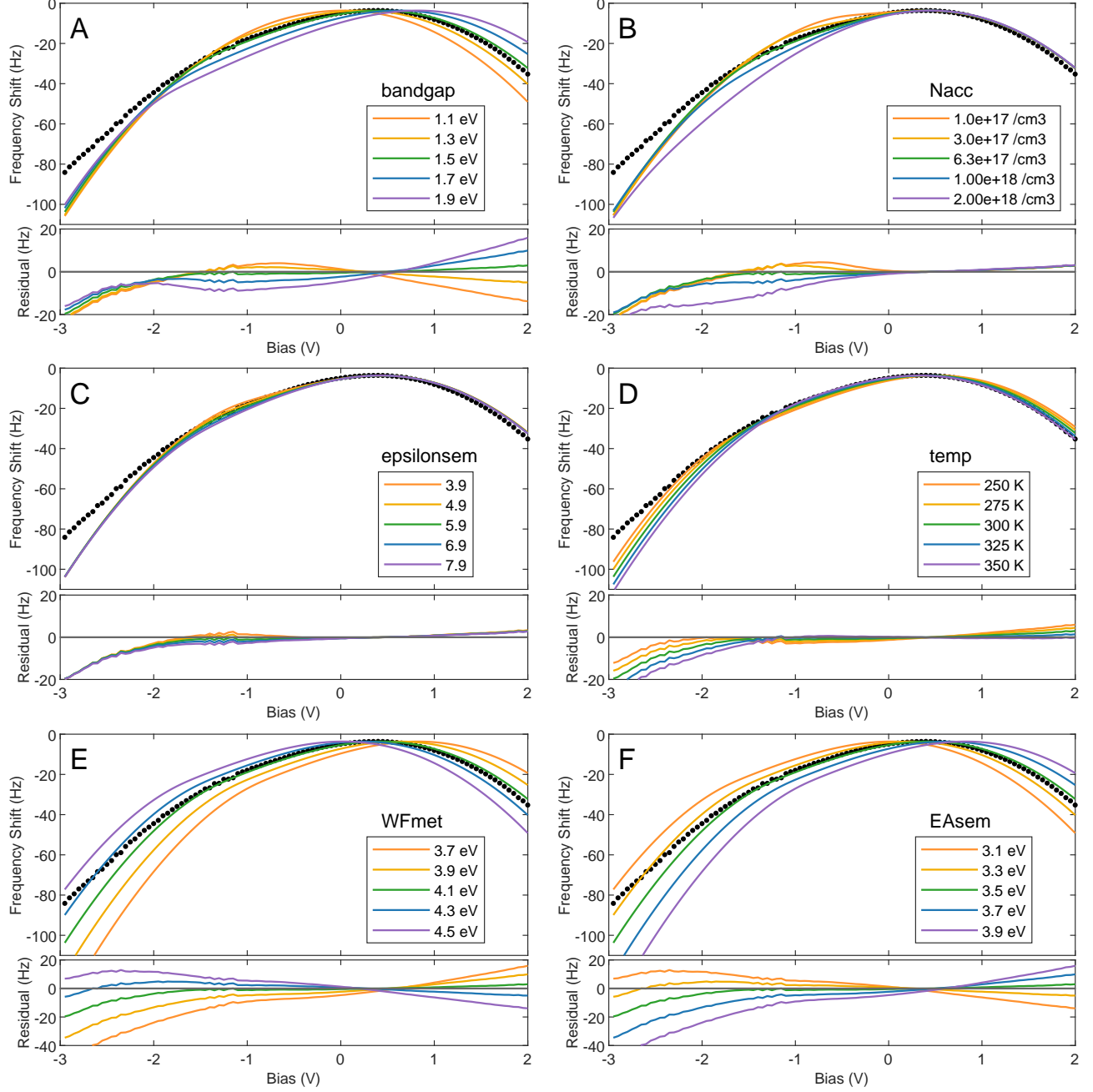


FIG. 6. Visualization of the sensitivity of generic MIS system fit parameters: a) band gap  $E_g$ ; b) Acceptor concentration  $N_A$ ; c) Permittivity  $\epsilon$ ; d) Temperature  $T$ ; e) Metal work function; f) Semiconductor electron affinity. The data from Figure 1 is shown in black. The best fit values are shown in green.

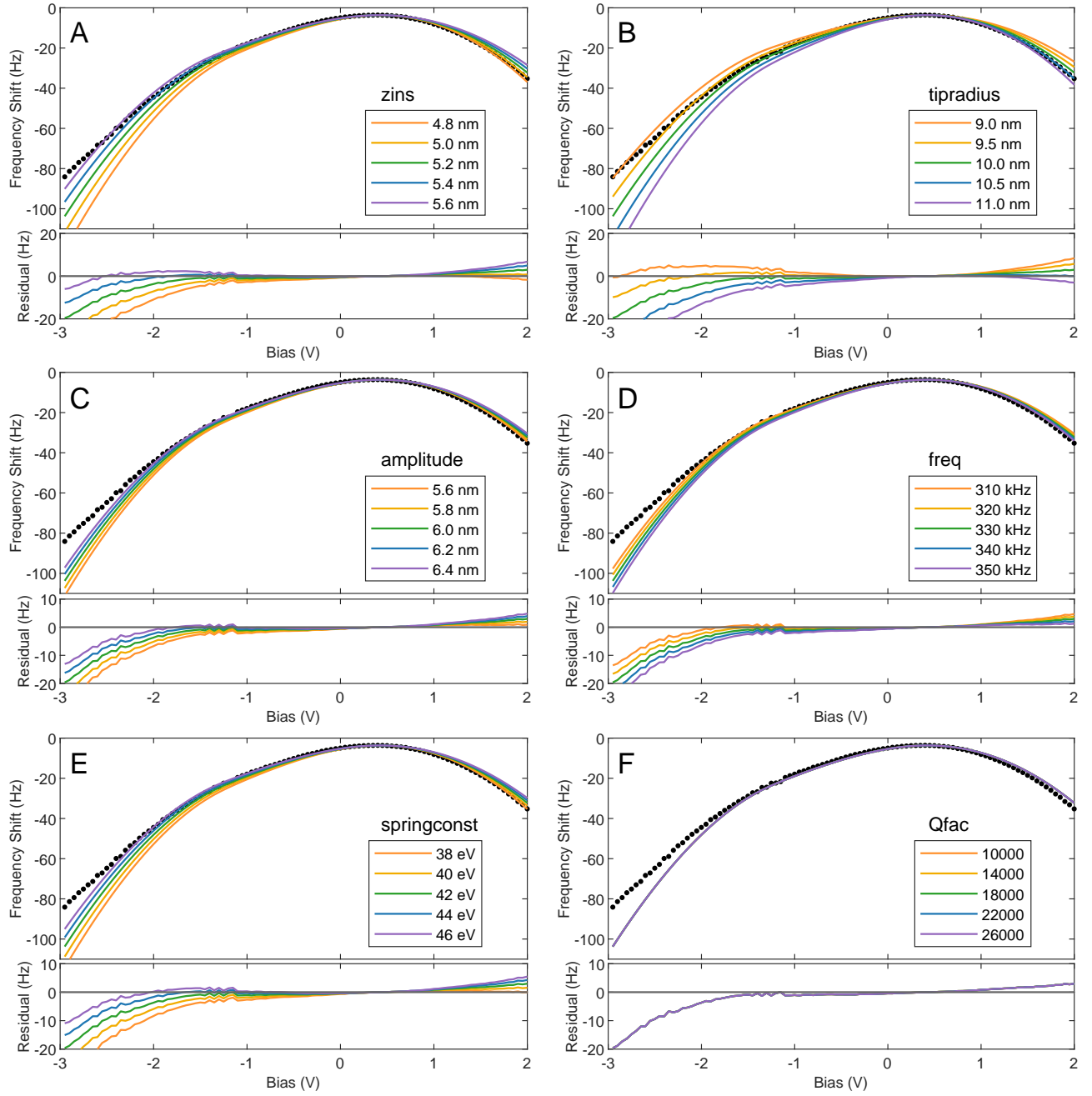


FIG. 7. Visualization of the sensitivity of fm-AFM-specific fit parameters (which are all multiplicative prefactors): a) tip-sample separation  $z_{ins}$ ; b) tip radius  $r_{tip}$ ; c) oscillation amplitude  $A$ ; d) oscillation frequency  $\omega$ ; e) spring constant  $k$ ; f) Q-factor  $Q$  (note that Q-factor curves are all perfectly overlapping). The data from Figure 1 is shown in black. The best fit values are shown in green.

## SUBSTRATE

Reference bias spectroscopy measurements were taken on the  $\text{SiO}_2$  substrate underlying the  $\text{MoSe}_2$  sample. The frequency shift, as compared to Figure 1b, is parabolic because Si has a comparatively small band gap of 1.1 eV (see Figure 6a) and a larger total insulator thickness ( $z_{ins}$ ) due to the  $\text{SiO}_2$  overlayer (see Figure 7a). (The larger  $z_{ins}$  also explains why the magnitude of the  $\text{SiO}_2$  frequency shift is much smaller than on  $\text{MoSe}_2$ .) The parabolic frequency shift indicates that there is very little charge reorganization occurring within the material. Therefore, the excitation, as compared to Figure 2 on  $\text{MoSe}_2$ , is constant on  $\text{SiO}_2$  because there no phase offset between the tip-sample position and the tip-sample force.

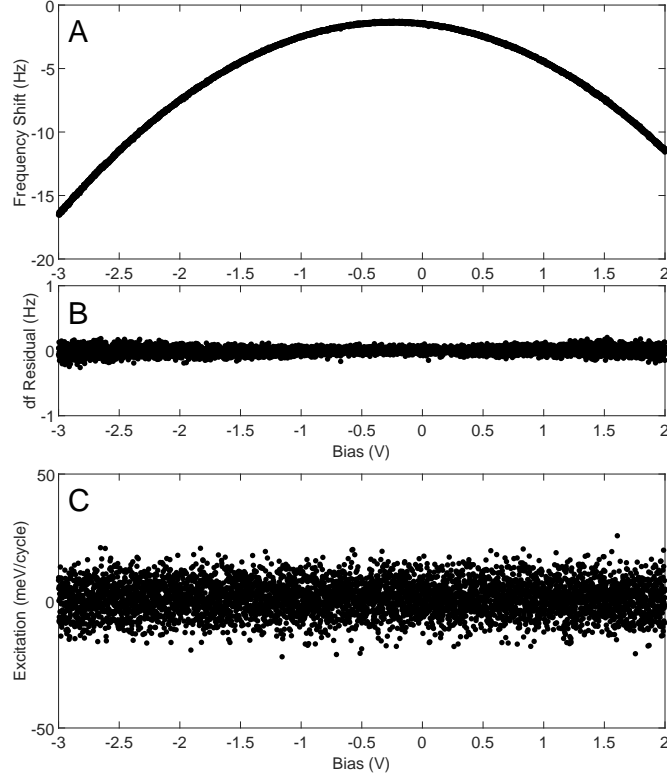


FIG. 8. a) Frequency shift measured on the  $\text{SiO}_2$  substrate. b) Residual of the frequency shift and a parabolic fit. c) Excitation measured simultaneously with the frequency shift shown in (a).

## DIFFERENCE PEAK

The difference between the ionized and un-ionized state frequency shift is bias-dependent. This gives rise to the bias-dependent frequency shift fluctuation amplitude shown in Figure 1c. This bias dependence is *not* due to a bias dependence of the dopant state, but rather is due to the transfer function of the fm-AFM measurement mechanism itself. This is demonstrated in Figure 9. Figures 9a-c show the surface potential as a function of tip-sample separation  $z_{ins}$  (dashed) and time (solid) at  $-2.2\text{ V}$ ,  $-1.4\text{ V}$ , and  $1.0\text{ V}$  for two different acceptor concentrations:  $6.3 \times 10^{17}/\text{cm}^3$  (black) and  $7.1 \times 10^{17}/\text{cm}^3$  (grey). Horizontal lines indicate the surface potential at the closest tip-sample position. Figures 9a-c show that, even though the magnitude of the surface potential swept at  $-2.2\text{ V}$  exceeds that of  $-1.4\text{ V}$ , the difference in surface potentials at the closest tip position is larger at  $-1.4\text{ V}$ . This is significant due to Equation 4a, which shows that the tip-sample force at the closest tip-sample position has the largest contribution to the frequency shift. The integrand from Equation 4a ( $F_{ts} \sin(\omega t)$ ) is found for each acceptor concentration, and their difference is plotted in Figures 9d-f (for  $-2.2\text{ V}$ ,  $-1.4\text{ V}$ , and  $1.0\text{ V}$ , respectively). Figure 9g shows the frequency shift as a function of bias (calculated using Equation 4a), and the biases corresponding to Figures 9a/d, b/e, and c/f ( $-2.2\text{ V}$ ,  $-1.4\text{ V}$ , and  $1.0\text{ V}$ ) are highlighted with vertical lines. This model, therefore, does not require any bias dependence in fluctuation frequency or amplitude. At biases corresponding to the parabola kink, where the surface potential slope is maximized, small variations in effective dopant concentration (due to, for example as in this case, thermally activated defect states) can create appreciable variations in the MIS capacitor force.

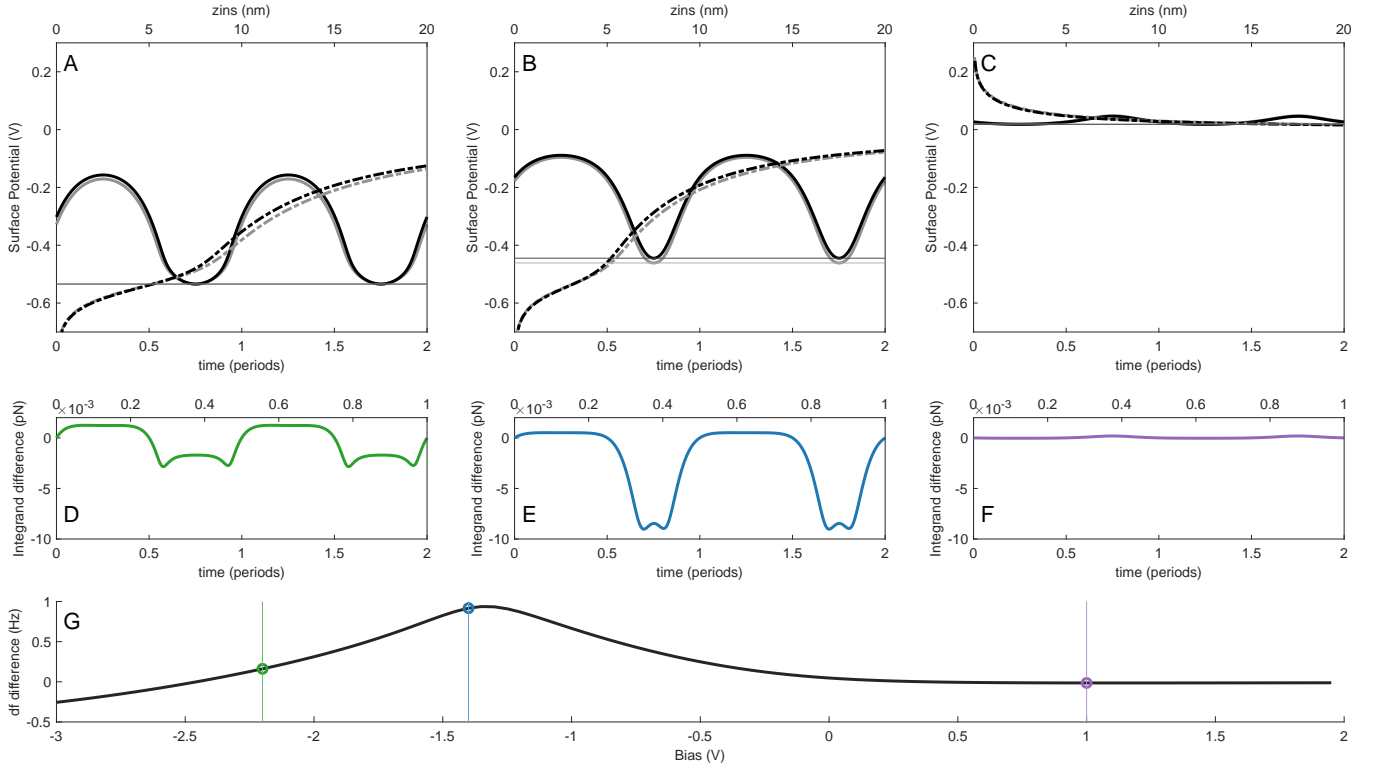


FIG. 9. a,b,c) The surface potential as a function of time (solid) and tip-sample separation  $z_{ins}$  (dashed) at  $-2.2\text{ V}$ ,  $-1.4\text{ V}$ , and  $1.0\text{ V}$ , respectively. Two different acceptor concentrations are shown:  $6.3 \times 10^{17}/\text{cm}^3$  (black) and  $7.1 \times 10^{17}/\text{cm}^3$  (grey). Horizontal lines are drawn to indicate the surface potential at the closest tip-sample separation. d,e,f) The force integrand needed to calculate frequency shift ( $F_{ts}(t) \sin(\omega t)$ , Equation 4a) difference between the two acceptor concentrations as a function of time. for  $-2.2\text{ V}$ ,  $-1.4\text{ V}$ , and  $1.0\text{ V}$ , respectively. g) The difference peak (also shown in Figure 1), calculated by integrating  $F_{ts}(t) \sin(\omega t)$  as a function of bias. The biases shown in d-f are shown highlighted with vertical lines.

## DASHBOARD & VIDEO

A dashboard allowing for interactive modification of all parameters can be found at <https://github.com/MeganCowie/SemiconductorsApp>. An attachment of the video is provided, and it is also available here: <https://youtu.be/YubyVw9h1Ms>